





Article

# Enhancement of Photocatalytic Rhodamine B Degradation over Magnesium–Manganese Baring Extracted Iron Oxalate from Converter Slag

Chitiphon Chuaicham <sup>1,\*</sup>, Jirawat Trakulmututa <sup>1</sup>, Sulakshana Shenoy <sup>1</sup>, Vellaichamy Balakumar <sup>2</sup>,  
Phatchada Santawaja <sup>3</sup>, Shinji Kudo <sup>3</sup>, Karthikeyan Sekar <sup>1,4</sup> and Keiko Sasaki <sup>1,\*</sup>

- <sup>1</sup> Department of Earth Resources Engineering, Kyushu University, Fukuoka 819-0395, Japan; palm@mine.kyushu-u.ac.jp (J.T.); sulakshana@mine.kyushu-u.ac.jp (S.S.); karthiks13@srmist.edu.in (K.S.)
- <sup>2</sup> Department of Chemistry, Sri Ramakrishna College of Arts & Science, Coimbatore 641006, Tamil Nadu, India; chembalakumar@gmail.com
- <sup>3</sup> Interdisciplinary Graduate School of Engineering Sciences, Institute for Materials Chemistry and Engineering, Kyushu University, Kasuga 816-8580, Japan; santawaja.p@gmail.com (P.S.); kudo.shinji.641@m.kyushu-u.ac.jp (S.K.)
- <sup>4</sup> Department of Chemistry, Faculty of Engineering and Technology, SRM Institute of Science and Technology, Kattankulathur 603203, Tamil Nadu, India
- \* Correspondence: song@mine.kyushu-u.ac.jp (C.C.); keikos@mine.kyushu-u.ac.jp (K.S.)

**Abstract:** In this work, iron oxalate from converter slag (FeOX-Slag) was produced by extraction of iron from converter slag using oxalic acid, followed by photo-reduction. The FeOX-Slag sample was subjected to various characterization techniques, including X-ray diffraction (XRD), Raman spectroscopy, scanning electron microscopy with energy-dispersive X-ray spectroscopy (SEM-EDX), ultraviolet–visible diffuse reflectance spectroscopy (UV-DRS), photoluminescence spectroscopy (PL), X-ray absorption near-edge structure spectroscopy (XANES), and X-ray photoelectron spectroscopy (XPS), in order to gain insights into its physicochemical properties. Also, to compare the photocatalytic activity of the FeOX-Slag, commercial iron oxide (Fe<sub>2</sub>O<sub>3</sub>) was used as a precursor to produce normal iron oxalate (FeOX-Fe<sub>2</sub>O<sub>3</sub>). The obtained FeOX-Slag was applied to the photocatalytic degradation of rhodamine B (RhB), a model organic contaminant in wastewater, compared with the FeOX-Fe<sub>2</sub>O<sub>3</sub>. Using the produced FeOX-Slag, we were able to degrade RhB more than 98% within 90 min at a reaction rate constant of about 3.6 times faster than FeOX-Fe<sub>2</sub>O<sub>3</sub>. Photoluminescence results confirmed the less recombination of the electron–hole pairs in FeOX-Slag, compared to FeOX-Fe<sub>2</sub>O<sub>3</sub>, which may be due to the defect structure of iron oxalate by guest metal impurities. The higher separation and transportation of photogenerated electron–hole pairs cause the enhancement of the degradation photocatalytic RhB degradation activity of the FeOX-Slag. In addition, The FeOX-Slag showed higher light absorption ability than FeOX-Fe<sub>2</sub>O<sub>3</sub>, resulting in the enhancement of the RhB degradation performance. Thus, the optical properties and the results from the activity tests led to the proposal that FeOX-Slag may be used in a photocatalytic degradation process for RhB under light irradiation.

**Keywords:** photocatalyst; RhB degradation; iron oxalate; converter slag



**Citation:** Chuaicham, C.; Trakulmututa, J.; Shenoy, S.; Balakumar, V.; Santawaja, P.; Kudo, S.; Sekar, K.; Sasaki, K. Enhancement of Photocatalytic Rhodamine B Degradation over Magnesium–Manganese Baring Extracted Iron Oxalate from Converter Slag. *Separations* **2023**, *10*, 440. <https://doi.org/10.3390/separations10080440>

Academic Editor: Fabio Gosetti

Received: 30 June 2023

Revised: 23 July 2023

Accepted: 1 August 2023

Published: 3 August 2023



**Copyright:** © 2023 by the authors. Licensee MDPI, Basel, Switzerland. This article is an open access article distributed under the terms and conditions of the Creative Commons Attribution (CC BY) license (<https://creativecommons.org/licenses/by/4.0/>).

## 1. Introduction

Converter slag is a solid byproduct of the steel manufacturing process. According to the World Steel Association’s global steel statistics for 2022, global crude steel production is over 1.95 billion metric tons. It indicates that the generation of converter slag has grown substantially as a result of 1 ton of crude steel yielding 10–15% slag [1,2]. However, the steel demand in 2023 was forecasted to increase by around 2.2% compared to 2021. In the past, massive amounts of steel slag were disposed in landfills, jeopardizing the natural

environment and human health owing to the leaching of heavy metals into soil and water by rainfall [3]. Therefore, the reduction of waste slag is a crucial issue for the industry.

Currently, steel slag is utilized in a variety of applications, such as road construction, civil engineering, and as an additive in cement or concrete [4–6]. The alternative method to reduce the amount of steel slag is metal recovery due to the ferrous content in steel slag, which is sustainable management. However, the chemical composition of steel slag contains CaO (41.55%), Fe<sub>2</sub>O<sub>3</sub> (31.35%), SiO<sub>2</sub> (11.47%), and other components (15.63%) [7]. There are several methods for metal extraction from the slag, i.e., flotation reagents, magnet separation, and chemical leaching [8]. To achieve high purity of Fe(III) oxalate solution, oxalic acid has been reported to be used as an extraction solvent [9,10]. This chemical (Fe<sub>2</sub>(C<sub>2</sub>O<sub>4</sub>)<sub>3</sub>) could be considered as the precursor to prepare the effective material for wastewater treatment, i.e., ferrous (II) oxalate (FeC<sub>2</sub>O<sub>4</sub>).

Fe(II) oxalate is a promising candidate for wastewater treatment in a variety of processes, including arsenic removal [11], organic pollutant degradation via Fenton reaction [12–14] or photocatalytic reaction [15,16], and Photo-Fenton process [17,18]. However, to achieve effective activity, Fenton or Photo-Fenton must use H<sub>2</sub>O<sub>2</sub> as an oxidant, which is an impractical and unsustainable process for real-world application. Therefore, the photocatalytic process is green, low cost, and uses mild conditions by harvesting the solar light power to chemical energy for complete mineralization [19–23]. For example, Hao et al. reported the degradation of organic dyes such as methylene blue and rhodamine B using C<sub>3</sub>N<sub>4</sub> composite via photocatalysis [21].

The aim of the present research is to synthesize Fe(II) oxalate through the extraction of iron from converter slag using oxalic acid and subsequently employing photo-reduction. Various analytical methods were employed to examine the physicochemical characteristics of the FeOX-Slag sample. In order to assess the photocatalytic efficacy of FeOX-Slag in relation to conventional iron oxalate, we employed iron oxide (Fe<sub>2</sub>O<sub>3</sub>) as a precursor for the synthesis of iron oxalate (FeOX-Fe<sub>2</sub>O<sub>3</sub>). In the framework of the photocatalytic degradation of rhodamine B (RhB), a representative organic pollutant found in wastewater, the FeOX-Slag, was utilized and compared to FeOX-Fe<sub>2</sub>O<sub>3</sub>.

## 2. Materials and Methods

### 2.1. Chemicals

For the process of synthesis as well as all experiments, the following chemicals were provided by Fujifilm Wako Pure Chemical Co. (Osaka, Japan): oxalic acid, iron(III) oxide (Fe<sub>2</sub>O<sub>3</sub>), p-benzoquinone (BQ), acetonitrile, isopropanol (IPA), and ethylenediaminetetraacetic acid disodium (EDTA-2Na). Rhodamine B (RhB) was procured from Sigma-Aldrich (St. Louis, MI, United States), a reputable supplier of chemicals. No additional purification steps were performed on any of the chemicals prior to their utilization. These solutions were prepared using ultrapure water, which is free from any impurities or contaminants.

### 2.2. Preparation of Iron Oxalate from Converter Slag (FeOX-Slag) and Iron Oxalate from Iron(III) Oxide (FeOX-Fe<sub>2</sub>O<sub>3</sub>)

The iron oxalate samples were synthesized through the dissolution of Fe from Fe sources (converter slag and iron(III) oxide), followed by the photo-reduction technique, as per the methodology described in the previous publication [10]. Particularly, a mass of 15 g of converter slag, also known as iron(III) oxide, was introduced into a 250-milliliter solution of oxalic acid with a concentration of 1 Molar. The aqueous mixture was agitated and subjected to thermal treatment at 100 °C under reflux conditions for a duration of 6 h. Subsequently, the solution containing Fe(III) oxalate in a dissolved state was effectively isolated from the residual solid matter through the process of filtration, employing a filter with a pore size of 0.45 μm. Subsequently, the solution containing Fe(III) oxalate was subjected to photo-reduction using a 100 W Hg lamp for a duration of 1 h. This process facilitated the reduction of the oxidation state of the Fe ion from Fe(III) to Fe(II) and

resulted in its precipitation as a solid. The composites acquired using distinct Fe sources, namely, converter slag and iron(III) oxide, were designated as FeOX-Slag and FeOX-Fe<sub>2</sub>O<sub>3</sub>, correspondingly.

### 2.3. Characterization

All materials' crystal phase structures were analyzed using an Ultima IV X-ray diffraction (XRD) instrument manufactured by RIGAKU, located in Akishima, Japan. To learn more about the chemical composition and functional groups of FeOX-Slag and FeOX-Fe<sub>2</sub>O<sub>3</sub>, we employed Raman spectroscopy (Thermo Scientific™ DXR3 Smart Raman spectrometer, Waltham, MA, USA). All samples were inspected using scanning electron microscopy (SEM, Hitachi High-Tech FlexSEM1000II, WITec K.K, Tokyo, Japan) to verify their morphology and surface properties. The evaluation of light absorption capabilities in both pure and composite materials was conducted using ultraviolet–visible diffuse reflectance spectroscopy (UV-DRS, UV-2450 Shimadzu, Kyoto, Japan). The VB positions of FeOX-Slag and FeOX-Fe<sub>2</sub>O<sub>3</sub> were determined through the utilization of X-ray photoelectron spectroscopy (XPS, ESCA 5800; ULVAC-PHI, Inc., Kanagawa, Japan). The PL spectroscopy measurements were conducted employing an FP-6600 spectrofluorometer (JASCO Corporation, Tokyo, Japan). The elemental compositions of all samples were determined via X-ray fluorescence (XRF) spectroscopy utilizing the Rigaku ZSX Primus II instrument in the wavelength dispersive mode, located in Akishima, Japan. Utilizing the Athena and Artemis software (version 0.9.26), specifically version 0.9.25, the spectral data obtained from the iron (Fe) K-edge was subjected to comprehensive analysis. In the investigation of RhB degradation products, the utilization of gas chromatography–mass spectrometry (GC–MS, Agilent 6890 N) with an HP-5MS UI column (Length = 30 m, = 0.250 mm) and helium gas as a carrier at a flow rate of 1 mL min<sup>-1</sup> was employed. The Fe K-edge XAS spectra of all samples were acquired at the SAGA Light Source (SAGA-LS) located at the BL06 Research Center for Synchrotron Light Application at Kyushu University.

### 2.4. Photocatalytic Rhodamine B (RhB) Removal

The ability to degrade rhodamine B (RhB) in the presence of visible light was used to evaluate the photocatalytic activity of FeOX-Slag and FeOX-Fe<sub>2</sub>O<sub>3</sub> under a 500 W Xe lamp. Each reaction started with 50 mg of the obtained FeOX-Slag or FeOX-Fe<sub>2</sub>O<sub>3</sub> suspended in 50 mL of 10 ppm RhB solution in the dark for 30 min to attain adsorption–desorption equilibrium. After that, the suspended liquid was irradiated from above with light from a 500W Xe lamp at a controlled reaction temperature of 25 °C. The remaining concentration of RhB in the treated solution was evaluated using UV/Vis Spectrophotometer at 554 nm, which is the maximum absorption ( $\lambda_{max}$ ) of the RhB molecule. The investigation of the presence and effect of free radicals was conducted through scavenger tests. One mole of p-benzoquinone (BQ), isopropanol (IPA), and ethylenediaminetetraacetic acid disodium (EDTA-2Na) were employed in the scavenger tests to eliminate super oxygen radicals, hydroxyl radicals, and holes. The tests were conducted using a 50 mL solution of 10 ppm RhB and 50 mg of the obtained catalyst. To ensure reusability, the exhausted catalyst from the preceding cycle was isolated from the solution via a centrifugal method and employed in its unmodified form, free of any purification processes.

## 3. Results and Discussion

### 3.1. Exploration of the Phase Composition and Chemical Characteristics

Figure 1a,b depicts the X-ray diffraction (XRD) analysis demonstrating the crystalline phase components of converter slag, FeOX-Slag, and FeOX-Fe<sub>2</sub>O<sub>3</sub>. Converter slag (Figure 1a) displayed (Mn,Mg)(Mn,Fe)<sub>2</sub>O<sub>4</sub> as the dominant phase, with main diffraction peaks at 18.2° and 35.5°. Also, some minor crystal phase components of calcium silicates, such as Ca<sub>2</sub>Fe<sub>1.4</sub>Mg<sub>0.3</sub>Si<sub>0.3</sub>O<sub>5</sub> and CaSi<sub>2</sub>O<sub>5</sub>, and iron(II) oxide (FeO) could be observed. The crystallographic phase structures of FeOX-Slag and FeOX-Fe<sub>2</sub>O<sub>3</sub> were subjected to X-ray diffraction (XRD) analysis, as depicted in Figure 1b. At temperatures of 18.6°, 20.9°, 22.9°,

28.4°, 29.3°, 34.5°, 37.9°, 40.1°, 42.7°, 44.7°, 46.1°, and 48.4°, the observed angles correlate with the orthorhombic crystal structure of iron oxalate dihydrate (JCPDS 01-076-4579), and two large distinct peaks of 002 plan at 18.6° were observed in both the FeOX-Slag and FeOX-Fe<sub>2</sub>O<sub>3</sub>. The experimental results demonstrate the successful synthesis of iron oxalate dihydrate through the efficient extraction of Fe from the two precursor compounds. However, the intensity of a main XRD peak at 18.6° of FeOX-Slag is lower than the FeOX-Fe<sub>2</sub>O<sub>3</sub>, suggesting the extracted Fe solution from converter slag that contains several components might contain some other elements and can be incorporated into the structure of the obtained FeOX-Slag, thereby resulting in a decrease in the crystallinity of the FeOX-Slag. To prove this assumption, the elemental compositions of FeOX-Slag and FeOX-Fe<sub>2</sub>O<sub>3</sub> were investigated using XRF analysis. It can be seen in Table 1 that the FeOX-Fe<sub>2</sub>O<sub>3</sub> contains only Fe, O, and C, which are from the backbone structure of the iron oxalate dehydrate, while the FeOX-Slag consists of Fe, O, and C as the main components from the structure of iron oxalate dehydrate and some impurities such as Mg and Mn from the converter slag precursor. Thus, this result suggests the co-doping of other impurities in the structure of iron oxalate dehydrate when converter slag was used as a precursor. Moreover, Raman spectroscopy was used to look into the chemical properties of FeOX-Slag and FeOX-Fe<sub>2</sub>O<sub>3</sub> as shown in Figure 1c. In the Raman spectrum of both samples, the  $\nu(\text{CO})$  modes of iron(II) oxalate can be observed at 1468 and 1454 cm<sup>-1</sup>. The two bands located at 582 and 579 cm<sup>-1</sup> correspond to the  $\delta(\text{CO}_2)$  mode of iron(II) oxalate. The peaks at 241 and 203 cm<sup>-1</sup> are consistent with an assignment to  $\nu(\text{FeO})$  modes, whereas the band at 114 cm<sup>-1</sup> corresponds to the  $\nu(\text{FeO}_2)$  mode of a coordinated metal–oxalate system [24]. Hence, these findings have substantiated the synthesis of iron oxalate dehydrate through the processes of extraction and photo-reduction employing the aforementioned precursors.

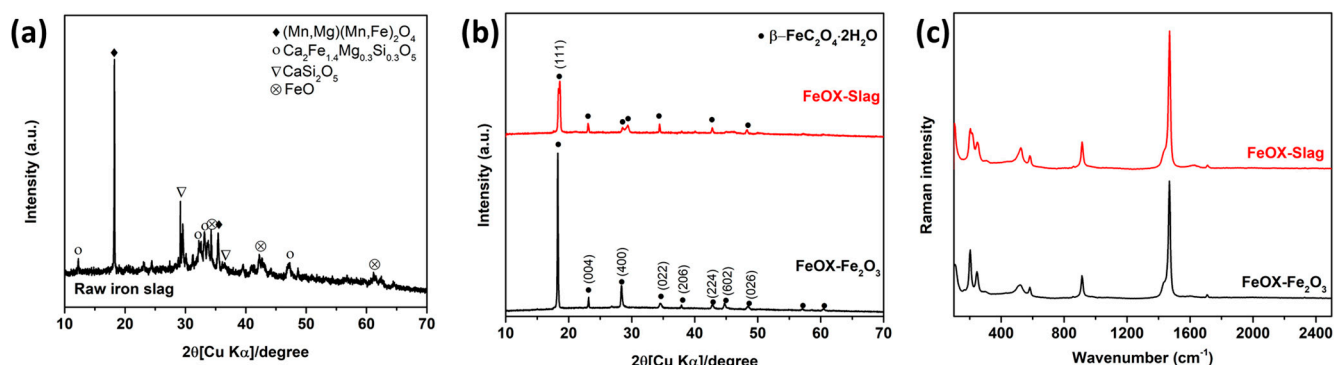


**Figure 1.** XRD patterns of (a) converter slag and (b) extracted FeOX-Fe<sub>2</sub>O<sub>3</sub> and FeOX-Slag and (c) Raman spectra of FeOX-Fe<sub>2</sub>O<sub>3</sub> and FeOX-Slag.

**Table 1.** Elemental component (%wt) using XRF analysis.

	C	O	Fe	Mg	Mn
FeOX-Fe <sub>2</sub> O <sub>3</sub>	26.4	66.3	7.3	n.d.	n.d.
FeOX-Slag	35.5	56.0	6.8	1.1	0.6

### 3.2. Optical Characteristics

UV-DRS spectroscopy was employed to elucidate the light absorption characteristics and the energy band gaps ( $E_g$ ) of FeOX-Slag and FeOX-Fe<sub>2</sub>O<sub>3</sub>, both of which play significant parts in the photo-catalytic steps. Figure 2a demonstrates the efficacy of both FeOX-Slag and FeOX-Fe<sub>2</sub>O<sub>3</sub> as proficient photocatalysts within the UV and visible light spectrum, showcasing maximum absorption between 300 and 550 nm. The ability to absorb visible and near-ultraviolet light by the FeOX-Slag was significantly higher compared to FeOX-Fe<sub>2</sub>O<sub>3</sub>. This meant that the optical characteristics of FeOX-Slag were improved by the addition of the Mg and Mn impurities to its structure. Its photocatalytic activity toward

RhB was improved, and its capacity to capture light was boosted, thanks to the large number of charge carriers it produced. The estimated  $E_g$  values of the FeOX-Slag and FeOX-Fe<sub>2</sub>O<sub>3</sub> samples were calculated using Tauc's equation [21,25–27]. Basically, iron oxalate was classified as an indirect semiconductor [28]. Thus, the  $E_g$  of the obtained sample are focused in the term of indirect  $E_g$ . The estimated  $E_g$  values for FeOX-Slag and FeOX-Fe<sub>2</sub>O<sub>3</sub> are 2.37 and 2.40 eV, respectively, as shown in Figure 2b. As compared to pure FeOX-Fe<sub>2</sub>O<sub>3</sub>, the  $E_g$  of FeOX-Slag was lower. This might be because the Mg and Mn impurities created new electronic states between the VB and CB. The photocatalytic performance of the obtained FeOX-Slag sample for RhB degradation may be enhanced due to the supplemented production of electron (e<sup>-</sup>) and hole (h<sup>+</sup>) pairs under light irradiation, as evidenced by the decreased  $E_g$  values of the composites [29,30].

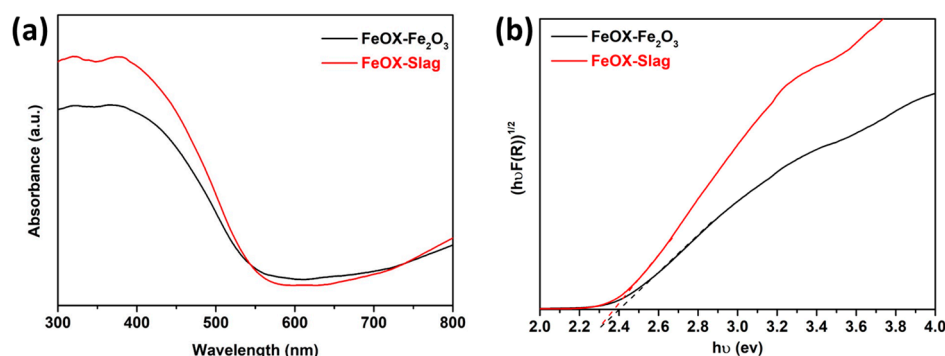


**Figure 2.** (a) UV–visible spectra and (b) Tauc's equation energy band gap plot of obtained FeOX-Slag and FeOX-Fe<sub>2</sub>O<sub>3</sub> samples.

### 3.3. Morphology Investigation

In Figure 3a,b, the SEM images of both FeOX-Slag and FeOX-Fe<sub>2</sub>O<sub>3</sub> samples clarify the surface morphologies and particle size. Intriguingly, the FeOX-Slag sample had less accumulation of the FeOX particles, suggesting that FeOX-Slag may provide a more responsive surface for photocatalytic RhB degradation than FeOX-Fe<sub>2</sub>O<sub>3</sub>. Excellent dispersion of Fe and O in the structure of the iron oxalate was shown using SEM-EDX mapping of both FeOX-Slag and FeOX-Fe<sub>2</sub>O<sub>3</sub> samples. The unambiguous indications of Fe and O elements in both FeOX-Slag and FeOX-Fe<sub>2</sub>O<sub>3</sub> samples suggested that these elements were the main constituents of iron oxalate, whereas the Mn and Mg signals were secondary. The regular distribution of Mn and Mg in the FeOX-Slag confirmed that they were co-doped in the structure of FeOX-Slag.

### 3.4. XPS Results

XPS was utilized to analyze the chemical states of C, Fe, and O, as well as the VB sites of FeOX-Slag and FeOX-Fe<sub>2</sub>O<sub>3</sub>. Figure 4a showed the survey spectra of FeOX-Slag and FeOX-Fe<sub>2</sub>O<sub>3</sub>. It can be seen that the signal of main elements such as Fe, C, and O can be observed for both samples; however, Mg and Mn, which are the minor elements in the FeOX-Slag, can be found due to the low concentration of these elements in the sample. The C 1s spectra of FeOX-Slag and FeOX-Fe<sub>2</sub>O<sub>3</sub> are given in Figure 4b, where the C 1s orbitals of FeOX-Slag and FeOX-Fe<sub>2</sub>O<sub>3</sub> may be deconvoluted into three peaks. The deconvoluted signal at 284.6 eV can be attributed to the C–C bond of contaminated carbon. The oxalate anion backbone in the iron oxalate was discovered to be responsible for the remaining two peaks at 285.8 and 288.5 eV [31]. It is feasible to discern two unique O 1s signals in Figure 4c, which are assigned to the various forms of O in the iron oxalate dehydrate. The peak corresponding to the C=O bond is observed at an energy level of 531.8 electron volts (eV), whereas the peak associated with H<sub>2</sub>O is detected at 532.4 eV [32]. Additionally, it is worth noting that the notable peak observed at EB [Fe 2p<sub>3/2</sub>] in Figure 4d exhibited a consistent energy value of 710 eV in both FeOX-Slag and FeOX-Fe<sub>2</sub>O<sub>3</sub> samples. This observation suggests that the Fe present in the iron oxalate structure exists in a trivalent

chemical state, thereby confirming the effective reduction of Fe(III) to Fe(II) through photo-reduction [33]. In addition, XPS was used to estimate the valence regions of FeOX-Slag and FeOX-Fe<sub>2</sub>O<sub>3</sub>. As can be shown in Figure 4e, the predicted VB sites of FeOX-Slag and FeOX are 1.27 and -0.28 eV, respectively. Interestingly, the VB position of FeOX-Slag slightly shifts down to a more positive side compared with FeOX-Fe<sub>2</sub>O<sub>3</sub>, indicating that the existence of the Mn and Mg as impurities affected the electronic properties of FeOX-Slag. The more positive level of the VB position of FeOX-Slag could promote the production of superoxide radical, which might be an important active species for RhB degradation. According to the UV-DRS data, the CB locations of FeOX-Slag and FeOX-Fe<sub>2</sub>O<sub>3</sub> were identified to be at -1.1 and -2.68 eV (Figure 4f), respectively.

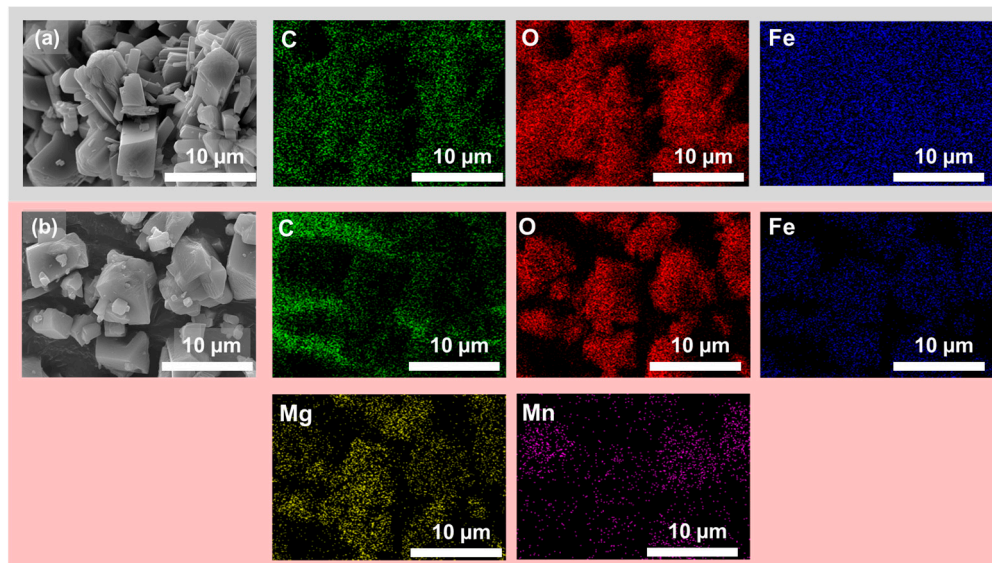


**Figure 3.** SEM images with two magnifications ( $\times 1500$  and  $\times 5000$ ) and EDX mapping of extracted iron oxalate from (a) FeOX-Slag and (b) FeOX-Fe<sub>2</sub>O<sub>3</sub>.

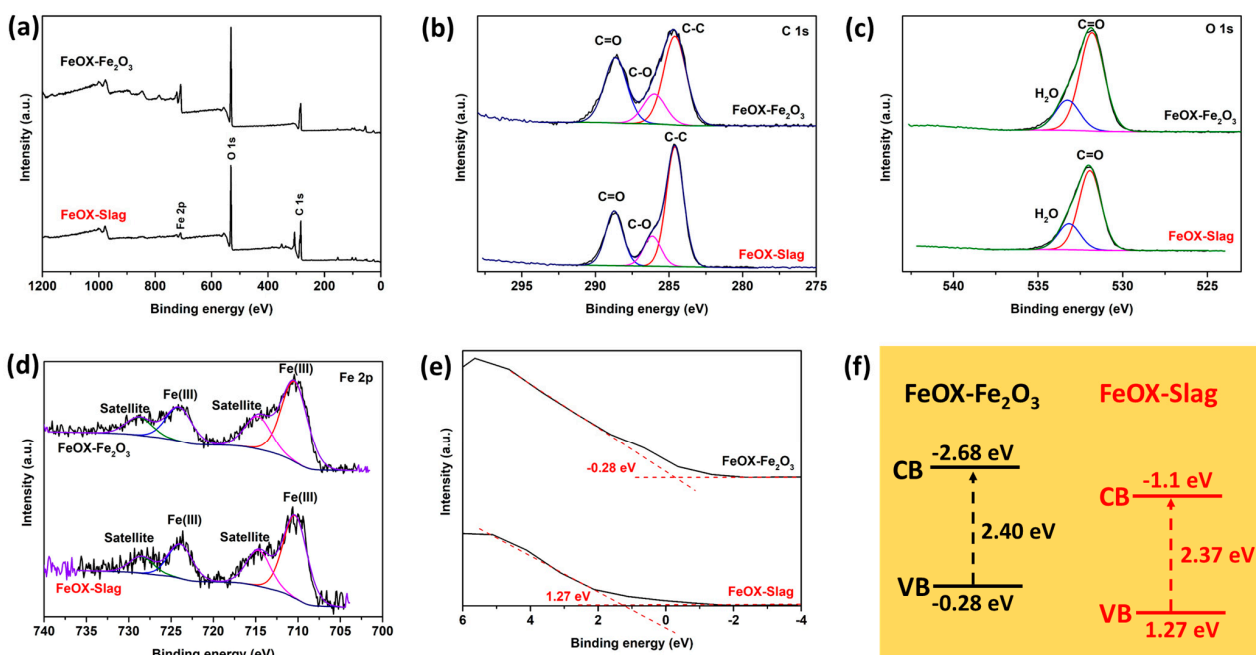


**Figure 4.** X-ray photoelectron spectra of isolated FeOX-Slag and FeOX-Fe<sub>2</sub>O<sub>3</sub>: (a) survey spectra, narrow scan spectra of (b) C 1s, (c) O 1s, (d) Fe 2p, (e) valence band energy region, and (f) diagram of electronic band position.

### 3.5. X-ray Absorption near Edge Structure (XANES) Result

As depicted in Figure 5, the acquired samples undergo X-ray absorption spectroscopy for the purpose of evaluation of oxidation state and phase configuration [34]. FeOX-Slag and FeOX-Fe<sub>2</sub>O<sub>3</sub> displayed comparable absorption edges at approximately 7125 eV and exhibited oscillation spectra following the edge jump, signifying the effective synthesis of iron oxalate using the oxalic acid-treated technique, without the presence of additional phase impurities such as iron oxide. Furthermore, it is noteworthy that the oxidation state of the iron (Fe) species in FeOX-Slag and FeOX-Fe<sub>2</sub>O<sub>3</sub> is divalent, as evidenced by the comparable binding energy observed between FeOX-Slag and FeOX-Fe<sub>2</sub>O<sub>3</sub> when compared to the iron oxalate standard.

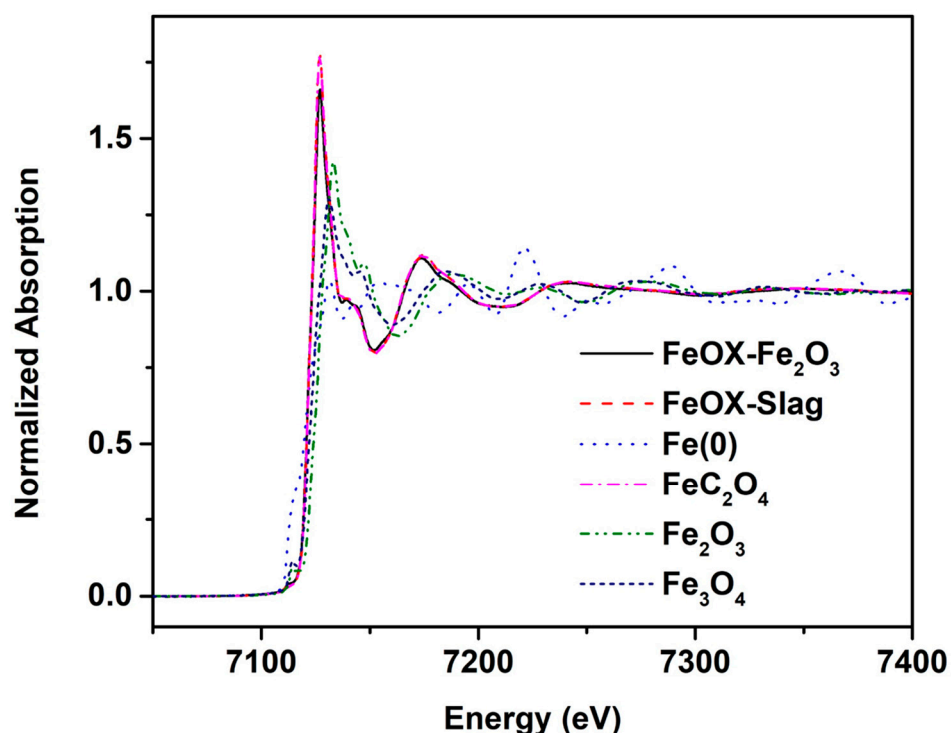
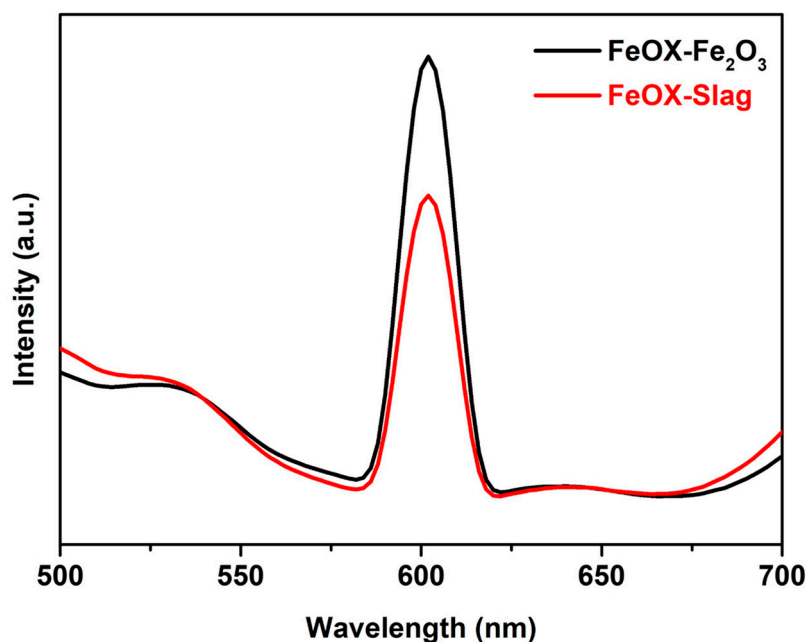


Figure 5. XANES spectra of FeOX-Slag and FeOX-Fe<sub>2</sub>O<sub>3</sub> and iron standards.

### 3.6. Charge Separation Properties

PL measurements were utilized to evaluate the impact of the preparation of iron oxalate using converter slag (FeOX-Slag) that contains some other impurities such as Mg and Mn on the separation and transfer of electrons and holes during light irradiation. As shown in Figure 6, the emission spectra of both FeOX-Slag and FeOX-Fe<sub>2</sub>O<sub>3</sub> samples are in the 500–700 nm region. Generally, a low PL intensity is indicative of a low rate of electron–hole pair recombinations. The distinct formulation of the FeOX-Slag, comprising additional impurities like Mg and Mn, resulted in enhanced charge carrier separation, as shown by the reduced PL emission intensity of FeOX-Slag in comparison to FeOX-Fe<sub>2</sub>O<sub>3</sub> at a wavelength of 600 nm under a 350 nm excitation. Based on the photoluminescence (PL) results, the electronic characteristics, encompassing charge separation and electron transport, exhibited enhancement due to the formation of Ets through the incorporation of impurities like Mg and Mn within the FeOX-Slag sample matrix.



**Figure 6.** PL spectra of FeOX-Slag and FeOX-Fe<sub>2</sub>O<sub>3</sub>.

### 3.7. Photocatalytic RhB Degradation

The decomposition of RhB under light irradiation was used to evaluate the photocatalytic activity of FeOX-Slag and FeOX-Fe<sub>2</sub>O<sub>3</sub>. In the absence of light, as depicted in Figure 7a, the adsorption efficacy for rhodamine B (RhB) in both FeOX-Slag and FeOX-Fe<sub>2</sub>O<sub>3</sub> specimens was approximately 25–30%. Interestingly, FeOX-Slag showed a higher adsorption capacity for RhB than that of pure FeOX-Fe<sub>2</sub>O<sub>3</sub>. This could potentially be attributed to the FeOX-Slag specimen exhibiting an elevated active surface area as a result of reduced agglomeration of FeOX-Slag particles. As a result, this makes it easier for the RhB molecules to connect with each other better. After that, all of the samples' decline efficiencies ( $C/C_0$ ) were tested to find out how well they worked as photocatalysts when exposed to light from a Xe lamp, which is a solar light simulator. After 90 min of response time, the  $C/C_0$  values of FeOX-Slag and FeOX-Fe<sub>2</sub>O<sub>3</sub> samples were 0.017 and 0.26. Therefore, the combined formation of iron oxalate through the extraction of Fe from converter slag exhibits greater potential for photocatalytic removal of RhB in comparison to regular FeOX-Fe<sub>2</sub>O<sub>3</sub>, owing to their heightened light absorption and charge separation capabilities. In detail, for photocatalytic RhB degrading activity, FeOX-Slag showed the highest level about 98% during the 90 min, while the FeOX-Fe<sub>2</sub>O<sub>3</sub> showed degradation activity of around 75% within the same reaction time. The FeOX-Slag's RhB degrading activity was dampened by an overabundance of the guest atoms. Furthermore, the rates of photocatalytic removal of RhB for FeOX-Slag and FeOX-Fe<sub>2</sub>O<sub>3</sub> were subjected to fitting based on experimental data employing a pseudo-first-order kinetic model, as depicted in Figure 7b. For FeOX-Slag and FeOX-Fe<sub>2</sub>O<sub>3</sub>, the corresponding values for the reaction rate constant ( $k$ ) were 0.012, and 0.043 min<sup>-1</sup>. FeOX-Slag had a rate constant that was two times higher than that of FeOX-Fe<sub>2</sub>O<sub>3</sub>. Therefore, our findings show that the FeOX-Slag's photocatalytic RhB degrading activity may be greatly enhanced by the creation of a new electronic state attained by doping with Mn and Mg. Based on the findings, it can be inferred that FeOX-Slag exhibits promising photocatalytic properties in the context of RhB degradation in wastewater, owing to its rapid kinetic rate and notable efficiency in RhB breakdown. Figure 7c shows how RhB can be removed by performing a photo-oxidation test without FeOX-Slag under light treatment and an adsorption test with FeOX-Slag under dark conditions. Photo-oxidation could lower the amount of RhB by about 5%. Also, the adsorption–desorption balance of RhB on the surface of the FeOX-Slag reached about 36% of removal activity within 15 min and stayed the same after that amount. The photocatalytic



process exhibited a significant reduction in RhB concentration, achieving a remarkable 98% decrease within a time frame of 90 min, indicating that RhB molecules are mostly removed through a photocatalytic process. Moreover, the role of radicals involved in the degradation of RhB was determined using a wide range of radical scavengers. In these scavenger experiments, isopropyl alcohol (IPA) and ethylenediaminetetraacetic acid disodium salt (EDTA-2Na) effectively captured superoxide anions ( $\bullet\text{O}_2^-$ ), hydroxyl radicals ( $\bullet\text{OH}$ ), and holes ( $\text{h}^+$ ). Upon the addition of BQ and EDTA-2Na, it was observed that the photocatalytic oxidation of RhB was diminished (Figure 7d), suggesting that the primary contributors to this phenomenon were  $\bullet\text{O}_2^-$  and  $\text{h}^+$ . Furthermore, the diminished degradation efficacy of FeOX-Slag in relation to RhB mineralization, when supplemented with IPA, signifies the involvement of  $\bullet\text{OH}$  as a secondary radical in the photocatalytic removal of RhB.

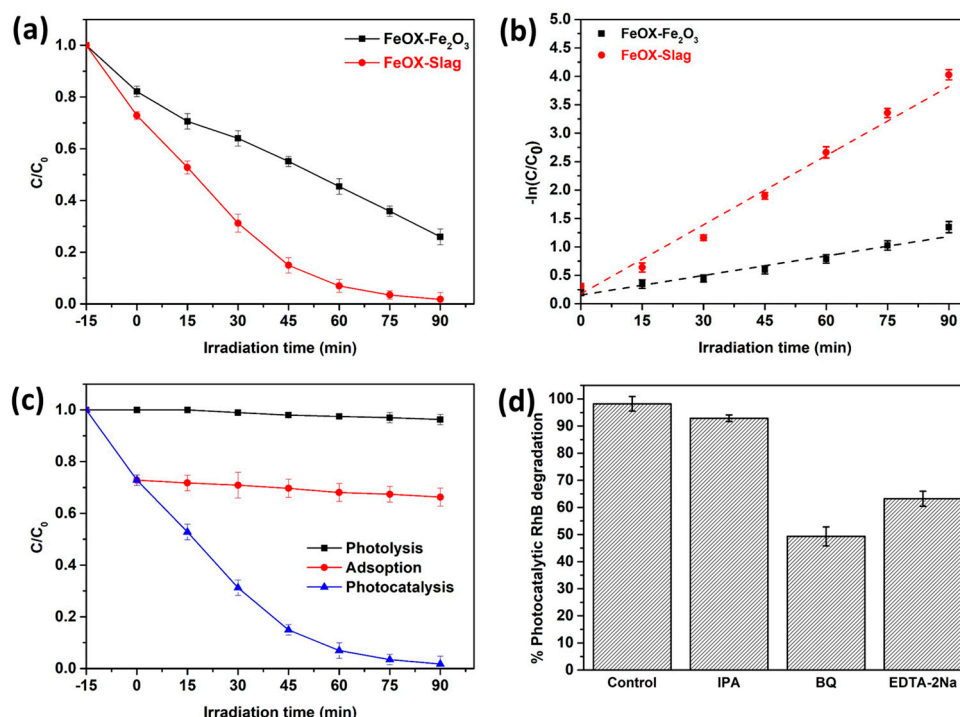


**Figure 7.** (a) Photocatalytic removal of RhB over FeOX-Slag and FeOX- $\text{Fe}_2\text{O}_3$ , (b) pseudo-first-order kinetics plot, (c) proof of RhB removal from FeOX-Slag, and (d) radical scavenger test.

### 3.8. Stability

The practical application of catalysts heavily relies on their stability and reusability [35]. The product's recyclable nature was evaluated throughout five cycles of FeOX-Slag for RhB degradation. The results depicted in Figure 8a indicate that FeOX-Slag exhibits high stability and recyclability in the context of RhB decomposition under light exposure. Specifically, the photocatalytic breakdown of RhB over FeOX-Slag remained consistent across five cycles, resulting in an impressive elimination rate exceeding 97% within a 90-min timeframe. XRD was used to evaluate the stability of FeOX-Slag following the first cycle of photocatalytic elimination of RhB to that of fresh slag. It can be seen in Figure 8b that the RhB deterioration did not affect the FeOX-Slag phase structures, as shown in comparison with the two diffraction patterns.

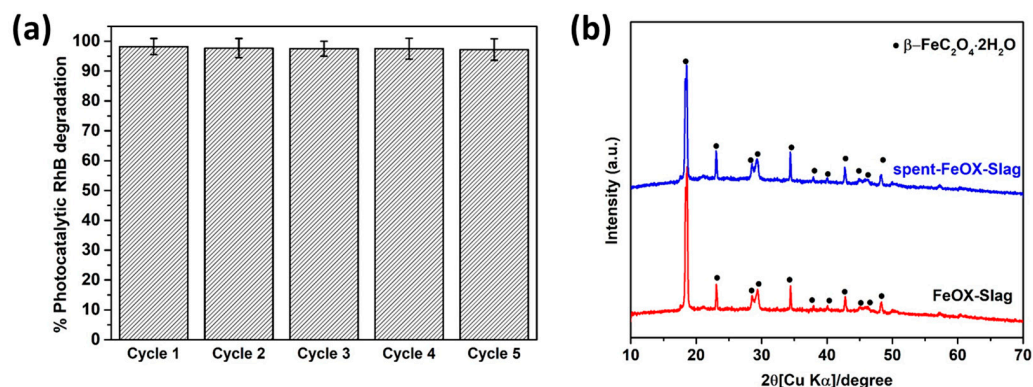


**Figure 8.** (a) Photocatalytic reusability FeOX-Slag for RhB removal and (b) XRD of spent FeOX-Slag comparing with FeOX-Slag.

3.9. Possible RhB Removal Process

In addition, after being exposed to light from the FeOX-Slag, the RhB concentration in the solution dropped dramatically, and some degraded product might be generated. Based on the results of gas chromatography–mass spectrometry (GC–MS) tests on RhB residues, Figure 9 shows a possible process for RhB oxidation. When the degraded solution was analyzed at 90 min after the photocatalytic process, it was found to have a lot of small pieces of RhB molecules (peaks with *m/z* values of 111, 118, 122, 132, 166, and 282). RhB molecules can be broken down into smaller, less dangerous molecules by using processes like N-demethylation, chromophore cleavage, and ring-opening to change their structure.

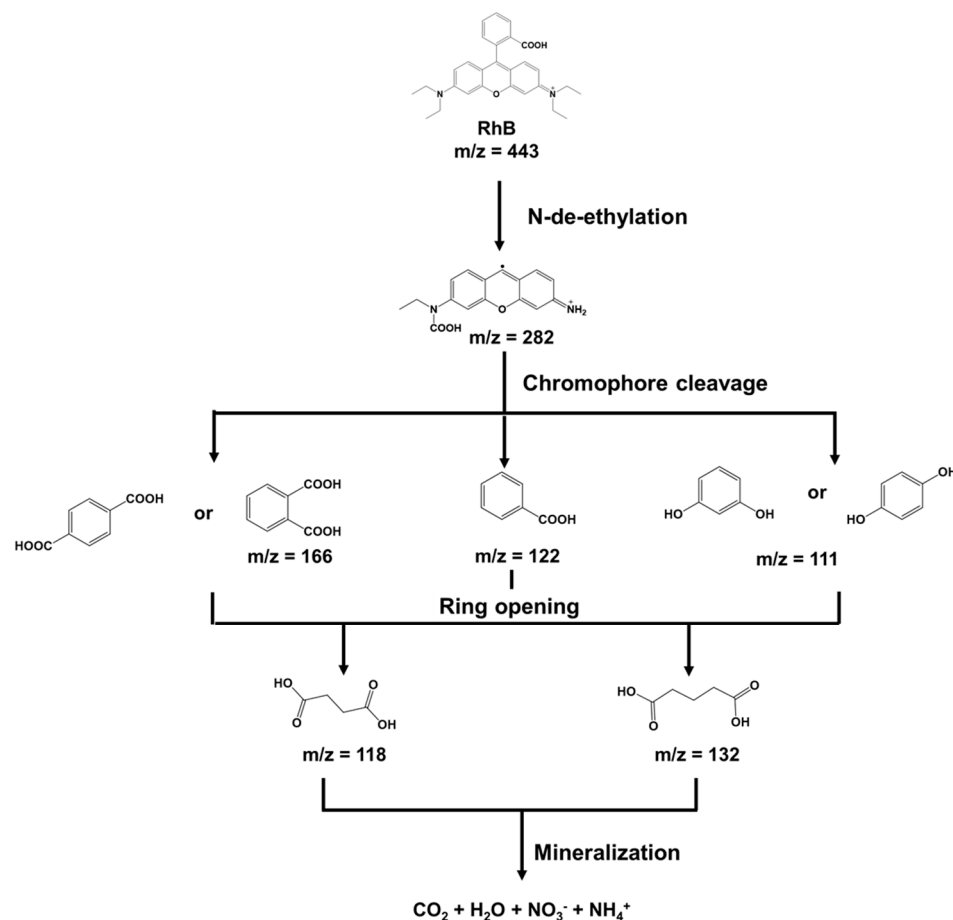


**Figure 9.** Possible RhB removal process using FeOX-Slag.

### 3.10. Photocatalytic Mechanism

Figure 10 depicts a proposed photocatalytic RhB mineralization process using FeOX-Slag, which is based on the results of this investigation. VB and CB of the FeOX-Slag were 1.27 and  $-1.1$  eV. Thus, FeOX-Slag produced electron-hole pair when exposed to light. Hole production in the VB occurred synchronously with the transportation of the excited electrons to the CB of the FeOX-Slag. The presence of Mn and Mg impurities within the FeOX-Slag has the potential to create a novel electronic state that can effectively capture and confine photogenerated electrons. The extended lifespan of charge carriers in the reaction was achieved by FeOX-Slag through the transfer of electrons to the newly formed electronic state induced by the presence of impurities. This process effectively prevented the recombination of photogenerated charge carriers. Consequently, the engagement between the electrons generated by light and the dissolved oxygen molecules in water led to the formation of superoxide radicals ( $\cdot\text{O}_2^-$ ) as a byproduct in the process of photocatalysis. Simultaneously, the presence of  $h^+$  in the valence band of the FeOX-Slag has the potential to directly oxidize and decompose RhB molecules into water ( $\text{H}_2\text{O}$ ). The two active radicals effectively facilitated the mineralization of RhB molecules, resulting in the formation of negligible quantities of non-toxic byproducts. Hence, the employment of converter slag for the synthesis of iron oxalate presents a promising approach in developing a highly effective photocatalyst for the mineralization of RhB. This is achieved through the enhancement of optical characteristics and the promotion of separation of charge carriers.

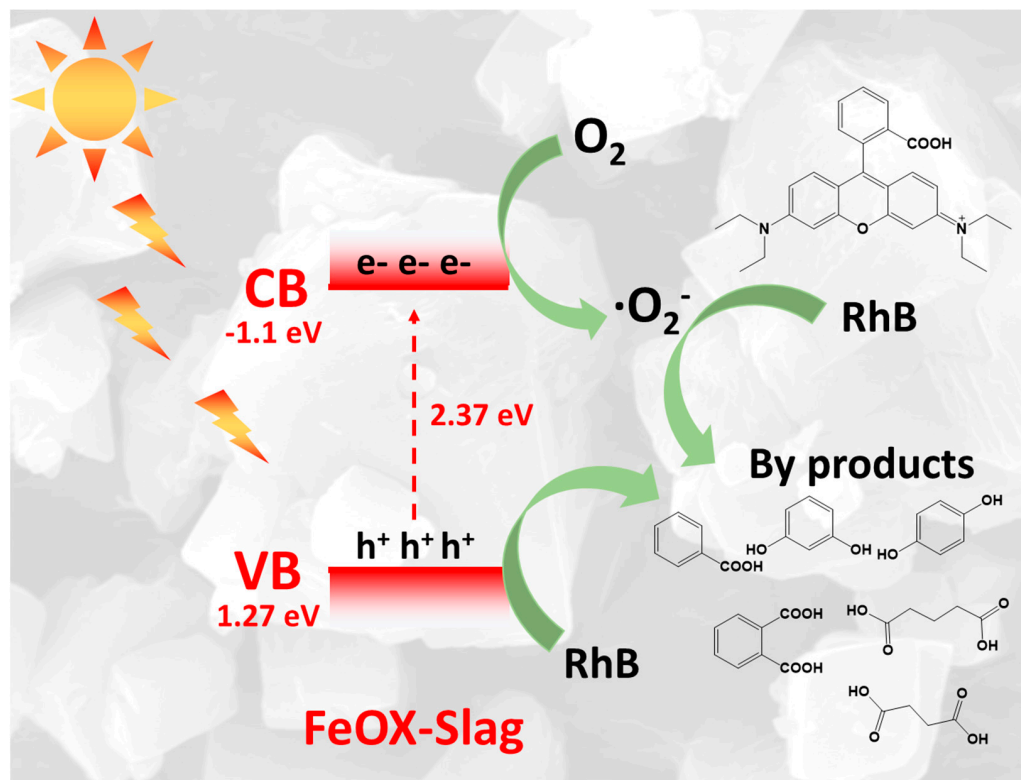


Figure 10. Schematic photocatalytic RhB removal using FeOX-Slag.

### 4. Conclusions

The utilization of an oxalic acid solution for the straightforward extraction of Fe from converter slag has the potential to yield iron oxalate, which can serve as a photocatalyst for the remediation of waste, specifically in the removal of RhB, an organic dye commonly found in wastewater. In this work, two types of iron oxalate were prepared using the difference of precursors,  $\text{Fe}_2\text{O}_3$  and converter slag. The obtained product using converter slag as a precursor (FeOX-Slag) demonstrated that the reaction rate constant for the effective degradation of RhB in wastewater was about two times higher than FeOX- $\text{Fe}_2\text{O}_3$ . FeOX-Slag also

outperformed all other reported photocatalysts in terms of photocatalytic RhB degradation. Based on the findings from UV-DRS and PL measurements, it can be concluded that the enhanced photocatalytic efficacy of FeOX-Slag in degrading RhB can be attributed to its superior light absorption capacity and reduced recombination of photo-generated charges. Some elements, like Mn and Mg, were added to FeOX-Slag, which decreased the combination of photogenerated charges. This made photocatalytic RhB degradation under light happen more efficiently. The photocatalyzed degradation products were also investigated using GC–MS analysis. Therefore, this research offers an alternative method to utilize the extracted Fe from converter slag for the effective treatment of wastewater polluted with organic contaminants under light irradiation.

**Author Contributions:** C.C.: Conceptualization, Investigation, Writing—original draft, and Writing—review and editing. C.C., S.S., J.T., V.B., P.S. and K.S. (Karthikeyan Sekar): Formal analysis. S.K., K.S. (Keiko Sasaki) and C.C.: Conception, Interpretation, and Editing the manuscript. All authors have read and agreed to the published version of the manuscript.

**Funding:** The work was supported by the Japan Society for the Promotion of Science (JSPS) KAKENHI (A) (No. JSPS JP22H00266) and Grant-in-Aid for Early-Career Scientists (project number = 23K17064). This work was partly supported by Advanced Research Infrastructure for Materials and Nanotechnology (grant number JPMXP1222KU1009), Japan, and sponsored by the Ministry of Education, Culture, Sports, Science and Technology (MEXT), Japan. This work was partly supported by 2022 Research Start Program 202208 to Chitiphon Chuaicham.

**Institutional Review Board Statement:** Not applicable.

**Informed Consent Statement:** Not applicable.

**Data Availability Statement:** Not applicable.

**Conflicts of Interest:** The authors declare no conflict of interest.

## References

1. Liu, T.; Wang, Y.; Li, J.; Yu, Q.; Wang, X.; Gao, D.; Wang, F.; Cai, S.; Zeng, Y. Effects from Converter Slag and Electric Arc Furnace Slag on Chlorophyll a Accumulation of *Nannochloropsis* sp. *Appl. Sci.* **2021**, *11*, 9127. [[CrossRef](#)]
2. Fusco, C.; Casiello, M.; Pisani, P.; Monopoli, A.; Fanelli, F.; Oberhauser, W.; Attrotto, R.; Nacci, A.; D'Accolti, L. Steel slag as low-cost catalyst for artificial photosynthesis to convert CO<sub>2</sub> and water into hydrogen and methanol. *Sci. Rep.* **2022**, *12*, 11378. [[CrossRef](#)]
3. Huo, B.; Li, B.; Huang, S.; Chen, C.; Zhang, Y.; Banthia, N. Hydration and soundness properties of phosphoric acid modified steel slag powder. *Constr. Build. Mater.* **2020**, *254*, 119319. [[CrossRef](#)]
4. Shu, K.; Sasaki, K. Occurrence of steel converter slag and its high value-added conversion for environmental restoration in China: A review. *J. Clean. Prod.* **2022**, *373*, 133876. [[CrossRef](#)]
5. Inoue, T.; Chuaicham, C.; Saito, N.; Ohtani, B.; Sasaki, K. Z-scheme heterojunction of graphitic carbon nitride and calcium ferrite in converter slag for the photocatalytic imidacloprid degradation and hydrogen evolution. *J. Photochem. Photobiol. A Chem.* **2023**, *440*, 114644. [[CrossRef](#)]
6. Zhang, Z.; Lü, H.; Li, X.; Li, X.; Ran, S.; Chen, Z.; Yang, Y.; Wu, X.; Li, L. Conversion of CaTi<sub>1-x</sub>Mn<sub>x</sub>O<sub>3-δ</sub>-Based Photocatalyst for Photocatalytic Reduction of NO via Structure-Reforming of Ti-Bearing Blast Furnace Slag. *ACS Sustain. Chem. Eng.* **2019**, *7*, 10299–10309. [[CrossRef](#)]
7. Liu, G.; Schollbach, K.; van der Laan, S.; Tang, P.; Florea, M.V.A.; Brouwers, H.J.H. Recycling and utilization of high volume converter steel slag into CO<sub>2</sub> activated mortars—The role of slag particle size. *Resour. Conserv. Recycl.* **2020**, *160*, 104883. [[CrossRef](#)]
8. Zhou, W.; Liu, X.; Lyu, X.; Gao, W.; Su, H.; Li, C. Extraction and separation of copper and iron from copper smelting slag: A review. *J. Clean. Prod.* **2022**, *368*, 133095. [[CrossRef](#)]
9. Liu, F.; Peng, C.; Wilson, B.P.; Lundström, M. Oxalic Acid Recovery from High Iron Oxalate Waste Solution by a Combination of Ultrasound-Assisted Conversion and Cooling Crystallization. *ACS Sustain. Chem. Eng.* **2019**, *7*, 17372–17378. [[CrossRef](#)]
10. Santawaja, P.; Kudo, S.; Mori, A.; Tahara, A.; Asano, S.; Hayashi, J.-I. Sustainable Iron-Making Using Oxalic Acid: The Concept, A Brief Review of Key Reactions, and An Experimental Demonstration of the Iron-Making Process. *ACS Sustain. Chem. Eng.* **2020**, *8*, 13292–13301. [[CrossRef](#)]
11. Kim, E.J.; Baek, K. Selective recovery of ferrous oxalate and removal of arsenic and other metals from soil-washing wastewater using a reduction reaction. *J. Clean. Prod.* **2019**, *221*, 635–643. [[CrossRef](#)]
12. Fu, L.; Huang, Z.; Zhou, X.; Deng, L.; Liao, M.; Yang, S.; Chen, S.; Wang, H.; Wang, L. Ferrous-Oxalate-Modified Aramid Nanofibers Heterogeneous Fenton Catalyst for Methylene Blue Degradation. *Polymers* **2022**, *14*, 3491. [[CrossRef](#)]

13. Lee, J.; Kim, J.; Choi, W. Oxidation of aquatic pollutants by ferrous-oxalate complexes under dark aerobic conditions. *J. Hazard. Mater.* **2014**, *274*, 79–86. [[CrossRef](#)]
14. Wang, G.; Zhou, A.; Xu, Q.  $\alpha$ -Ferrous oxalate with different micro scale: Synthesis and catalytic degradation effect to rhodamine B. *Solid State Sci.* **2019**, *91*, 54–60. [[CrossRef](#)]
15. Sarmah, K.; Pratihari, S. Synthesis, Characterization, and Photocatalytic Application of Iron Oxalate Capped Fe, Fe–Cu, Fe–Co, and Fe–Mn Oxide Nanomaterial. *ACS Sustain. Chem. Eng.* **2016**, *5*, 310–324. [[CrossRef](#)]
16. Liu, Z.-J.; Liu, W.; Wang, Y.; Guo, M.-L. Preparation of  $\beta$ -ferrous oxalate dihydrate layered nanosheets by mechanochemical method and its visible-light-driven photocatalytic performance. *Mater. Lett.* **2016**, *178*, 83–86. [[CrossRef](#)]
17. Conde-Morales, I.I.; Hinojosa-Reyes, L.; Guzmán-Mar, J.L.; Hernández-Ramírez, A.; Sáenz-Tavera, I.d.C.; Villanueva-Rodríguez, M. Different Iron Oxalate Sources as Catalysts on Pyrazinamide Degradation by the Photo-Fenton Process at Different pH Values. *Water Air Soil Pollut.* **2020**, *231*, 425. [[CrossRef](#)]
18. Luo, Z.; Min, Y.; Qu, L.; Song, Y.; Hong, Y. Remediation of phenanthrene contaminated soil by ferrous oxalate and its phytotoxicity evaluation. *Chemosphere* **2021**, *265*, 129070. [[CrossRef](#)]
19. Chuaicham, C.; Trakulmututa, J.; Shu, K.; Shenoy, S.; Sriksaow, A.; Zhang, L.; Mohan, S.; Sekar, K.; Sasaki, K. Recent Clay-Based Photocatalysts for Wastewater Treatment. *Separations* **2023**, *10*, 77. [[CrossRef](#)]
20. Trakulmututa, J.; Chuaicham, C.; Shenoy, S.; Sriksaow, A.; Sasaki, K.; Smith, S.M. Effect of transformation temperature toward optical properties of derived CuO/ZnO composite from Cu–Zn hydroxide nitrate for photocatalytic ciprofloxacin degradation. *Opt. Mater.* **2022**, *133*, 112941. [[CrossRef](#)]
21. Hao, D.; Huang, Q.; Wei, W.; Bai, X.; Ni, B.-J. A reusable, separation-free and biodegradable calcium alginate/g-C<sub>3</sub>N<sub>4</sub> microsphere for sustainable photocatalytic wastewater treatment. *J. Clean. Prod.* **2021**, *314*, 128033. [[CrossRef](#)]
22. Balu, S.; Chuaicham, C.; Balakumar, V.; Rajendran, S.; Sasaki, K.; Sekar, K.; Maruthapillai, A. Recent development on core-shell photo(electro)catalysts for elimination of organic compounds from pharmaceutical wastewater. *Chemosphere* **2022**, *298*, 134311. [[CrossRef](#)]
23. Shanmugam, M.; Augustin, A.; Mohan, S.; Honnappa, B.; Chuaicham, C.; Rajendran, S.; Hoang, T.K.A.; Sasaki, K.; Sekar, K. Conducting polymeric nanocomposites: A review in solar fuel applications. *Fuel* **2022**, *325*, 124899. [[CrossRef](#)]
24. Edwards, H.G.M.; Russell, N.C. Vibrational spectroscopic study of iron(II) and iron(III) oxalates. *J. Mol. Struct.* **1998**, *443*, 223–231. [[CrossRef](#)]
25. Makuła, P.; Pacia, M.; Macyk, W. How To Correctly Determine the Band Gap Energy of Modified Semiconductor Photocatalysts Based on UV–Vis Spectra. *J. Phys. Chem. Lett.* **2018**, *9*, 6814–6817. [[CrossRef](#)]
26. Chuaicham, C.; Inoue, T.; Balakumar, V.; Tian, Q.; Ohtani, B.; Sasaki, K. Visible light-driven ZnCr double layer oxide photocatalyst composites with fly ashes for the degradation of ciprofloxacin. *J. Environ. Chem. Eng.* **2022**, *10*, 106970. [[CrossRef](#)]
27. Chuaicham, C.; Sekar, K.; Balakumar, V.; Mittraphab, Y.; Shimizu, K.; Ohtani, B.; Sasaki, K. Fabrication of graphitic carbon nitride/ZnTi-mixed metal oxide heterostructure: Robust photocatalytic decomposition of ciprofloxacin. *J. Alloys Compd.* **2022**, *906*, 164294. [[CrossRef](#)]
28. Keshavarz, F.; Kadek, M.; Barbiellini, B.; Bansil, A. Anodic Activity of Hydrated and Anhydrous Iron (II) Oxalate in Li-Ion Batteries. *Condens. Matter* **2022**, *7*, 8.
29. Balakumar, V.; Manivannan, R.; Chuaicham, C.; Karthikeyan, S.; Sasaki, K. A simple tactic synthesis of hollow porous graphitic carbon nitride with significantly enhanced photocatalytic performance. *Chem. Commun.* **2021**, *57*, 6772–6775. [[CrossRef](#)]
30. Pawar, R.R.; Chuaicham, C.; Sekar, K.; Rajendran, S.; Sasaki, K. Synthesis, characterization, and application of MOF@clay composite as a visible light-driven photocatalyst for Rhodamine B degradation. *Chemosphere* **2022**, *291*, 132922. [[CrossRef](#)]
31. Chenakin, S.; Kruse, N. Thermal Decomposition of Nickel Oxalate Dihydrate: A Detailed XPS Insight. *J. Phys. Chem. C* **2019**, *123*, 30926–30936. [[CrossRef](#)]
32. Li, Y.; Wu, H.; Wu, Y.; Li, Q. Facile synthesis of mesoporous Co<sub>3</sub>O<sub>4</sub> nanowires for application in supercapacitors. *J. Mater. Sci. Mater. Electron.* **2017**, *28*, 16826–16835. [[CrossRef](#)]
33. Li, L.; Ma, P.; Hussain, S.; Jia, L.; Lin, D.; Yin, X.; Lin, Y.; Cheng, Z.; Wang, L. FeS<sub>2</sub>/carbon hybrids on carbon cloth: A highly efficient and stable counter electrode for dye-sensitized solar cells. *Sustain. Energy Fuels* **2019**, *3*, 1749–1756. [[CrossRef](#)]
34. Tian, Q.; Guo, B.; Chuaicham, C.; Sasaki, K. Mechanism analysis of selenium (VI) immobilization using alkaline-earth metal oxides and ferrous salt. *Chemosphere* **2020**, *248*, 126123. [[CrossRef](#)]
35. Sriksaow, A.; Smith, S.M.; Uraisin, K.; Suttiponparnit, K.; Kongmark, C.; Chuaicham, C. Catalytic remediation of phenol contaminated wastewater using Cu–Zn hydroxide nitrate. *RSC Adv.* **2016**, *6*, 36766–36774. [[CrossRef](#)]

**Disclaimer/Publisher’s Note:** The statements, opinions and data contained in all publications are solely those of the individual author(s) and contributor(s) and not of MDPI and/or the editor(s). MDPI and/or the editor(s) disclaim responsibility for any injury to people or property resulting from any ideas, methods, instructions or products referred to in the content.